CORA Cork Open Research Archive
Cartlann Taighde Oscailte Chorcaí

Title	Cu-Doped TiO2: Visible light assisted photocatalytic antimicrobial activity
Authors	Mathew, Snehamol;Ganguly, Priyanka;Rhatigan, Stephen;Kumaravel, Vignesh;Byrne, Ciara;Hinder, Steven J.;Bartlett, John;Nolan, Michael;Pillai, Suresh C.
Publication date	2018-10-26
Original Citation	Mathew, S., Ganguly, P., Rhatigan, S., Kumaravel, V., Byrne, C., Hinder, S., Bartlett, J., Nolan, M. and Pillai, S., 2018. Cu-doped TiO2: visible light assisted photocatalytic antimicrobial activity. Applied Sciences, 8(11), (2067). DOI:10.3390/app8112067
Type of publication	Article (peer-reviewed)
Link to publisher's version	https://www.mdpi.com/2076-3417/8/11/2067 - 10.3390/app8112067
Rights	© 2018 by the authors. Licensee MDPI, Basel, Switzerland - https://creativecommons.org/licenses/by/4.0/
Download date	2026-11-04 22:01:23
Item downloaded from	https://hdl.handle.net/10468/8433

UCC
University College Cork, Ireland
Coláiste na hOllscoile Corcaigh

applied sciences

MDPI

Article

Cu-Doped TiO_2: Visible Light Assisted Photocatalytic Antimicrobial Activity

Snehamol Mathew [1,2], Priyanka Ganguly [1,2], Stephen Rhatigan [3], Vignesh Kumaravel [1,2], Ciara Byrne [1,2], Steven J. Hinder [4], John Bartlett [1], Michael Nolan [3,*] and Suresh C. Pillai [1,2,*]

1 Nanotechnology and Bio-engineering Research Group, Department of Environmental Science, Institute of Technology Sligo, Sligo F91 YW50, Ireland; Snehamol.Mathew@mail.itsligo.ie (S.M.); Priyanka.Ganguly@mail.itsligo.ie (P.G.); Kumaravel.Vignesh@itsligo.ie (V.K.); Ciara.Byrne@mail.itsligo.ie (C.B.); bartlett.john@itsligo.ie (J.B.)
2 Centre for Precision Engineering, Materials and Manufacturing Research (PEM), Institute of Technology Sligo, Sligo F91 YW50, Ireland
3 Tyndall National Institute, University College Cork, Lee Maltings, Dyke Parade, Cork P51 DX59, Ireland; stephen.rhatigan@tyndall.ie
4 The Surface Analysis Laboratory, Faculty of Engineering and Physical Sciences, University of Surrey, Guildford, Surrey GU2 7XH, UK; s.hinder@surrey.ac.uk
* Correspondence: michael.nolan@tyndall.ie (M.N.); pillai.suresh@itsligo.ie (S.C.P.)

Received: 27 September 2018; Accepted: 22 October 2018; Published: 26 October 2018



Abstract: Surface contamination by microbes is a major public health concern. A damp environment is one of potential sources for microbe proliferation. Smart photocatalytic coatings on building surfaces using semiconductors like titania (TiO_2) can effectively curb this growing threat. Metal-doped titania in anatase phase has been proven as a promising candidate for energy and environmental applications. In this present work, the antimicrobial efficacy of copper (Cu)-doped TiO_2 (Cu-TiO_2) was evaluated against *Escherichia coli* (Gram-negative) and *Staphylococcus aureus* (Gram-positive) under visible light irradiation. Doping of a minute fraction of Cu (0.5 mol %) in TiO_2 was carried out via sol-gel technique. Cu-TiO_2 further calcined at various temperatures (in the range of 500–700 °C) to evaluate the thermal stability of TiO_2 anatase phase. The physico-chemical properties of the samples were characterized through X-ray diffraction (XRD), Raman spectroscopy, X-ray photo-electron spectroscopy (XPS) and UV–visible spectroscopy techniques. XRD results revealed that the anatase phase of TiO_2 was maintained well, up to 650 °C, by the Cu dopant. UV–vis results suggested that the visible light absorption property of Cu-TiO_2 was enhanced and the band gap is reduced to 2.8 eV. Density functional theory (DFT) studies emphasize the introduction of Cu^+ and Cu^{2+} ions by replacing Ti^{4+} ions in the TiO_2 lattice, creating oxygen vacancies. These further promoted the photocatalytic efficiency. A significantly high bacterial inactivation (99.9999%) was attained in 30 min of visible light irradiation by Cu-TiO_2.

Keywords: Cu-doped TiO_2; doping; phase transition; *Escherichia coli*; *Staphylococcus aureus*; photocatalysis; antibacterial coatings

1. Introduction

The formation of microbial colonies inside the wet or damp indoor environments is one of the major contributing elements to the deterioration of indoor air quality [1,2]. These microorganisms have the potential to produce contaminants like spores, allergens and toxins affecting the health of the occupants [3,4]. This kind of continuous exposure can lead to various health concerns like respiratory or skin diseases [5,6]. Several studies in the past few decades have looked at the alteration of building materials and paints to overcome the challenges of indoor microbial contamination [7,8]. Most of the

physicochemical techniques and usual cleaning procedures are inactive to completely eliminate the microbes. Photocatalysis is one of the most promising, simple and economically viable technology to address indoor air microbial contamination [9].

Existing photocatalyst-based coatings suffer two important disadvantages, they require artificial UV light sources to generate reactive oxygen species (ROS) and secondly these coatings remain inactive in dark atmosphere as the ROS generated in light declines with time [10]. TiO_2 has been recognized as a traditional semiconductor photocatalyst, which has been widely reported for its anti-microbial coatings [11,12]. The formation of uniform aqueous slurry and the feasibility of deposition on the various substrates make TiO_2 a lucrative candidate [13,14]. However, this material suffers from its own set of limitations. Among the three phases of TiO_2, anatase is reported to be the most photocatalytically active phase [15]. However, the phase stability of anatase is very crucial as it has a tendency to rutilation at elevated temperatures. Apart from this, low visible light absorption because of the wide band gap of TiO_2 (3.2 eV) is incompatible to receive visible light for practical applications [16].

Elemental doping, morphological tailoring in the form of nanotubes and fibers, making composites out of new 2-D materials like graphene, C_3N_4, are some of the efficient techniques to overcome these limitations [17–20]. Earlier studies on heterojunctions of anatase-rutile and anatase-brookite for photocatalytic applications have been reported. Although anatase is the photocatalytically active phase, the heterojunctions formed in the mixed phase samples showed superior photocatalytic activity under visible light [21,22]. It is attributed to the delayed charge recombination initiated by the electron-hole separation effect [22]. Elemental doping is an effective strategy to tune the band gap of TiO_2 by introducing new energy levels in between and by alteration of conduction band minima (CBM) and valence band maxima (VBM) [23,24]. In this regard, cationic dopants served to extend the visible light absorption and also enhanced the high temperature stability of the anatase phase TiO_2. Copper is one of the interesting dopants added to TiO_2 at the different mole and weight percent. Cu-doped TiO_2 was evaluated for various photocatalytic applications like Hydrogen production [25–28], CO_2 conversion [29], degradation of dyes and organic contaminants. Kim et al. reported that Cu existed in the form of both Cu^+ and Cu^{2+} states in Cu-doped TiO_2 thin films. These nano-architectures showed higher activity for degradation of organic dye molecules under visible light illumination [30]. Similarly, Varghese et al., demonstrated high CO_2 conversion to hydrocarbon fuels using Cu incorporated TiO_2 nanotube arrays [31]. In another study, authors explored the electronic and structural stability of Cu-doped TiO_2 synthesized in different acidic mediums (HNO_3 and H_2SO_4). The doped sample calcined at 600 °C displayed high photocatalytic activity for phenol degradation [32]. Several studies demonstrating the photocatalytic anti-bacterial efficiency were also reported (Table S1) [33–40]. However, in most of the cases, a high concentration of Cu was used to display the antimicrobial activity and did not study the effect of calcination temperature. They either calcined at a single temperature or kept the temperature below that of the anatase-rutile phase transition. So, this work provides new insights into higher temperature anatase phase stability of Cu-doped TiO_2. Additionally, Cu dopants were deposited on morphologically tuned TiO_2 nanotubes and nanofibers. This involves a series of cumbersome synthesis techniques.

In the present study, we demonstrate a facile one-step sol-gel technique to prepare 0.5 mol % of Cu-TiO_2. The as-prepared samples were calcined at different temperatures ranging from 500 to 700 °C. Density Functional Theory (DFT) simulations were also performed to understand any bandgap alteration of TiO_2 lattice and the formation of oxygen vacancies after Cu doping. The anatase phase of TiO_2 was maintained (55%) up to 650 °C. The sample calcined at 650 °C illustrated high visible light absorption, and Cu doping resulted in lowering of TiO_2 band gap from 3.2 eV (for anatase TiO_2) to 2.8 eV. Cu-TiO_2 was further assessed for the photocatalytic disinfection efficiency towards *Escherichia coli* (Gram-negative) and *Staphylococcus aureus* (Gram-positive) bacterial strains. A 5-Log reduction by the Cu-TiO_2 was attained at a very short time span of 30 min.

2. Materials and Methods

2.1. Chemicals and Reagents

All the materials used were of analytical grade. The materials were used as received, without further purification. Titanium isopropoxide (97%), copper sulphate pentahydrate (≥98.0%) and isopropanol (≥99.5%) were purchased from Sigma-Aldrich. Strains of *Staphylococcus aureus* (ATCC-25923) and *Escherichia coli* (ATCC-25922) were purchased from LGC Standards. Nutrient broth No.2, Agar and all other consumables were bought from Cruinn Diagnostics Ltd (Dublin, Ireland). Deionized water was used in all experiments.

2.2. Synthesis of Cu-TiO_2

Cu-TiO_2 was synthesized using a sol-gel method as follows: 40 mL of titanium isopropoxide (TTIP) was stirred in isopropanol (200 mL) for 15 min (solution A). The required amount of copper sulphate was taken separately in deionized water (200 mL) and the mixture was stirred for 15 min (solution B). The ratio of both solvents was kept constant. Then, Solution B was added dropwise to solution A under vigorous stirring. After that, the mixture was further kept for gelation for 2 h at room temperature. The resulting gel was dried in an oven at 100 °C for 12 h. The powder was then calcined at various temperatures (500 °C, 600 °C, 650 °C and 700 °C) at a ramp rate of 10 °C/min for 2 h. Pure TiO_2 was also synthesized by the same procedure without the addition of copper sulphate and calcined at two different temperatures (500 °C and 700 °C) to obtain pristine anatase and rutile samples, respectively. These samples were used as the control for all further experiments.

2.3. Density Functional Theory (DFT) Computations

DFT calculations were performed using the VASP5.2 [41,42] code with projector augmented wave (PAW) [43,44] potentials to account for the core–valence interaction and a kinetic energy cut-off of 400 eV. Cu was substitutionally doped onto a Ti site in an anatase (4 × 4 × 3) supercell. This gives a dopant percentage of ~0.5%, which is consistent with the experimental concentrations of Cu in TiO_2 [25,32,45]. Γ-point sampling was used and structures were relaxed until forces were less than 0.01 eV $Å^{-1}$.

Calculations were performed taking into account spin polarization and no symmetry constraints were imposed. For DFT calculations corrected for onsite Coulomb interactions (DFT + U), U = 4.5 eV was applied to the Ti 3d states and U = 7 eV was applied to the Cu 3d states, arising from the inability of the local density and generalized gradient approximations to consistently describe both Ti^{3+} and Cu^{2+} oxidation states [46,47]. These choices for U are based on previous studies [48–52]. In addition, the DFT + U correction was applied to the O 2p states, as a result of the hole states formed when substituting the lower valance Cu cation on a Ti site [53]. Comparisons of the DFT + U results were made for these systems with no +U correction. However, this set-up is unable to consistently describe the oxygen hole states and the Ti^{3+} and Cu^{2+} oxidation states of the cations and thus results are not shown for this computational set-up. The starting geometries were manually distorted from the symmetric bulk geometry in order to examine relaxation to distorted geometries, which can be compared with undistorted geometries. To study the charge compensation that arises as a result of the difference in the Cu^{2+} and Ti^{4+} oxidation states, one oxygen ion was removed from different sites of the most stable Cu-doped structures and the energy of formation was calculated by the following equation:

$$\mathrm{Evac} = \mathrm{E}\left(\mathrm{Cu_xTi_{1-x}O_{2-y}}\right) + \frac{1}{2}\mathrm{E}(\mathrm{O_2}) - \mathrm{E}(\mathrm{Cu_xTi_{1-x}O_2}) \quad (1)$$

where $\mathrm{E}\left(\mathrm{Cu_xTi_{1-x}O_{2-y}}\right)$ is the total energy of Cu-doped TiO_2 with a charge compensating oxygen vacancy and $\mathrm{E}(\mathrm{Cu_xTi_{1-x}O_2})$ is the total energy of Cu-doped TiO_2. The formation energy is referenced to half the total energy of O_2.

Copper ions were initially in the 2+ oxidation state and calculations were therefore performed with 1 and 3 unpaired spins taking into account the electron deficit due to substitutional doping of Cu^{2+} for Ti^{4+} and the d9 configuration of Cu^{2+}. The oxidation states of Cu dopant, lattice Ti and O ions were determined from Bader charge analysis [54].

2.4. Characterization

The as-synthesized samples were characterized by various techniques. The crystallinity of the samples was analyzed by X-ray diffraction (XRD). The diffractograms were produced using Cu Kα radiation (λ = 0.15418 nm) in a Siemens D500 X-ray powder diffractometer (Karlsruhe, Germany). The diffraction was examined in the range of 10°–80°. Anatase and rutile percentages of TiO_2 were measured by the Spurr equation [15].

$$F_R = \frac{1}{1 + 0.8[I_A(101)/I_R(110)]} \quad (2)$$

where F_R is the quantity of rutile phase; $I_A(101)$ and $I_R(110)$ are the intensity of anatase peak and rutile peak respectively. The crystallinity of the samples was calculated using the Scherrer equation [55].

$$\Phi = \frac{K\lambda}{\beta \cos\theta} \quad (3)$$

where Φ is the crystallite size; K is the shape factor with a value close to unity; λ is the wavelength of X-rays; β is the full width half-maximum (FWHM) of the main intensity peak; and θ is the Bragg angle.

The phase transformation was also analyzed using Raman spectroscopy (Horiba Jobin Yvan LabRAM HR 800, Villeneuve d'Ascq, France) with a grating of 300 gr/mm. A 660 nm solid state diode laser standard bandwidth version with double edge filter upgrade was the laser used. The acquisition time was 3 s.

The bonding interactions and oxidation state of elements were studied with the help of X-ray photoelectron spectroscopy. XPS analyses were performed on a ThermoFisher Scientific Instruments (East Grinstead, UK) K-Alpha+ spectrometer. XPS spectra were acquired using a monochromated Al Kα X-ray source (hn = 1486.6 eV). An X-ray spot of ~400 μm radius was employed. Survey spectra were acquired employing a Pass Energy of 200 eV. High resolution, core level spectra for all elements were acquired with a Pass Energy of 50 eV. All spectra were charge referenced against the C1s peak at 285 eV to correct for charging effects during acquisition. Quantitative surface chemical analyses were calculated from the high resolution, core level spectra following the removal of a non-linear (Shirley) background. The manufacturers' Avantage software was used which incorporates the appropriate sensitivity factors and corrects for the electron energy analyzer transmission function.

The optical properties of the as prepared samples were measured using a Perkin-Elmer UV–Vis Spectrophotometer (Beaconsfield, Buckinghamshire, UK) Barium sulphate ($BaSO_4$) was used as a reference, and slit width was set to 1 nm. Additionally, band gap was calculated from the UV DRS spectrum by using Kubelka-Munk function F(R) [56].

$$F(R) = \frac{(1-R)^2}{2R} \quad (4)$$

where R is the absolute reflectance of the sample.

The photocatalytic experiments were performed inside a weathering and corrosion photo-reactor (Q-sun Xe-1-S) from Q-Labs (Saarbrucken, Germany).

2.5. Measurement of Antimicrobial Activity

All the glassware used was autoclaved before carrying out the photocatalytic experiments. *E. coli* (Gram-negative bacterium) and *S. aureus* (Gram-positive bacterium) were used to study the

antibacterial activity of the Cu-TiO_2. Nutrient broth culture medium was prepared by dissolving 25 g of nutrient broth No.2 (10 g peptone, 5.0 g NaCl, 10 g beef extract) in 1 L of distilled water followed by sterilization at 121 °C using an autoclave. The 90 mm agar plates were prepared by dissolving 28 g nutrient agar (5 g peptone, 8.0 g NaCl, 3.0 g Beef extract, Agar No. 2) in 1 L distilled water, then autoclaved at 121 °C for 15 min and poured into petri dishes. The strains were inoculated in 20 mL of nutrient broth and incubated for 24 h at 37 °C. A definite amount of the grown culture was transferred to the cylindrical glass vessel to make the working solution of 10^4 CFU/mL (colony forming unit/mL). The reaction mixture was kept inside the photo test chamber for visible light irradiation. The photocatalyst concentration was fixed at 1 g/L and irradiated for 3 h. Aliquots of 1 mL were extracted out from the reaction mixture at a regular time interval of 10 min. In order to attain a countable CFU, the bacterial solution was diluted in a PBS solution once and later 100 µL of the diluted solution was plated. Finally, the plates were incubated at 37 °C for 24 h. The colonies formed on the agar plates were counted and recorded as CFU/mL. A control experiment was also conducted in the absence of the photocatalyst. The same set of samples was tested simultaneously under dark conditions. The antimicrobial efficiency was calculated using two methods; (i) log reduction and (ii) N/N_0% versus time.

$$\log \text{ reduction } = \log_{10} \frac{(A)}{(B)} \Rightarrow \log_{10} (A) - \log_{10} (B) \quad (5)$$

where, A = initial number of viable microorganisms, B = number of viable microorganisms at any time "t", $\log_{10}$ (A) $\rightarrow N_0$, $\log_{10}$ (B) $\rightarrow$ N for any time "t".

3. Results

3.1. Density Functional Theory Simulations

There have been some theoretical papers on the topic of Cu-doped anatase TiO_2 [57–60]. A DFT + U study [59] of anatase doped with Cu at a concentration of 6.25%, applied U = 8 eV to the Ti 3d states; this recovers the bulk TiO_2 energy gap but is not to be recommended for other properties. No +U correction is applied to the Cu 3d states, despite issues with describing these electronic states. A reduction in the band gap was reported in all studies and this is attributed to a combination of Cu 3d and O 2p states above the valence band maximum (VBM). Navas et al. provided a comprehensive study [58] of Cu-doping in anatase which combined both experiment and theory including DFT + U calculations with the +U correction on Ti 3d orbitals only. However, the inclusion of a +U correction for Cu 3d states is particularly important in correctly describing the Cu^{2+} oxidation state [48,49,61]. They reported greater band gap reduction with increases in dopant concentration due to the covalent character of the Cu-O interaction leading to new states at the VBM. DFT studies have examined the impact of Cu-doping of the anatase (101) surface [62,63] with a focus on surface mediated phenomena in catalysis. A generalized gradient approximation (GGA) study showed that Cu dopants at the anatase (101) surface inhibit the dissociation of adsorbed water to hydroxyls [62]. The authors attributed enhancements in the photocatalytic activity to arise instead from the electronic properties and inter-bandgap states, rather than the promotion of water dissociation. A GGA + U study found little difference in the formation energies for substitutional doping of Cu at surface and sub-surface Ti sites [63] suggesting both are equally favorable. The emergence of impurity levels in the TiO_2 bandgap led to a predicted red shift in light absorption compared to unmodified TiO_2. A theoretical account of Cu-doping in rutile, in the context of the effect of oxygen vacancies on the magnetic moment of Cu-doped TiO_2 [64], reported that oxygen vacancies are most stable near the Cu impurity.

Figure 1a shows the local atomic structure in the vicinity of the Cu dopant. The geometry around the dopant is symmetric in which apical Cu-O and equatorial Cu-O distances are 2.01 Å and 1.99 Å; these can be compared with corresponding Ti-O distances of 2.02 Å and 2.00 Å for undoped anatase. Figure 1b displays the excess spin density plot and shows that the hole states are spread over the

oxygen sites neighboring the dopant. The computed spin magnetizations are 0.13 μ_B for both apical sites and 0.2 μ_B for the four equatorial sites. The Bader charge of the Cu dopant is 9.6 electrons and the spin magnetization is 0.97 μ_B, consistent with the d^9 configuration of the Cu^{2+} oxidation state.

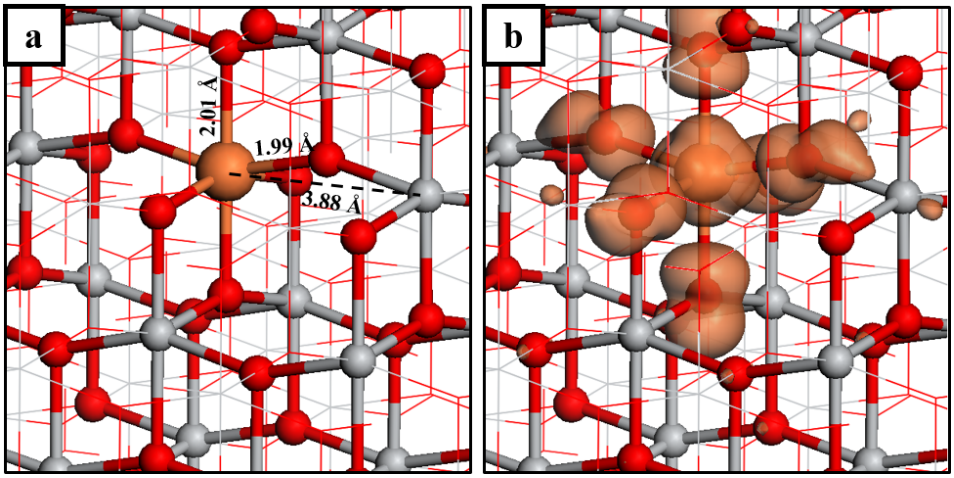


Figure 1. (**a**) Relaxed atomic structure of bulk anatase TiO_2 in the vicinity of the Cu dopant and (**b**) excess spin density plot for Cu-doped anatase TiO_2. Spin isosurfaces enclose densities of up to 0.02 eV/Å^3. In this and subsequent figures Ti is represented by a grey sphere, O by a red sphere and Cu by an orange sphere.

For the solution with the +U correction applied to the O 2p states, the local atomic structure near the dopant site is distorted asymmetrically; this set up results in localization of the hole states predominantly on the apical oxygen sites and the resulting Cu-O_{Ap} distances are 2.27 Å and 2.42 Å. These elongated bonds are consistent with formation of an oxygen polaron as has been observed in other materials [46,47,65–69]. The computed spin magnetizations for these O sites are 0.78 μ_B and 0.73 μ_B and the Bader charges are reduced by 0.5 electrons after hole localization, from 7.3 to 6.8 electrons. The four equatorial Cu-O_{Eq} distances are 1.99–2.00 Å. For the remainder of the calculations the differences arising from U(O) = 0 eV vs. U(O) = 7 eV are quantitative in nature and the general characteristics of Cu-doped anatase are consistent, in particular charge compensation. Thus, for brevity we include only the results arising from calculations for which U(O) = 0 eV.

In response to the charge imbalance which arises when replacing Ti^{4+} with lower valent Cu^{2+}, the system compensates through formation of an oxygen vacancy. The most stable site for this compensating oxygen vacancy is the O site neighboring the Cu dopant in the equatorial position and this has a computed formation energy of −0.35 eV.

The top panels of Figure 2 show the geometry of the charge compensated system in the vicinity of the Cu dopant; the oxygen vacancy site is indicated by a black circle. After formation of the charge compensating oxygen vacancy, the Cu and Ti ions to which the removed O atom was bound have five-fold coordination. The Ti ions move off their lattice sites and outwards from the vacancy site and this distortion leads to the shortening of metal-oxygen bonds opposite the vacancy by 0.13–0.16 Å. After oxygen vacancy formation, four of the Cu-O bonds contract by 0.01–0.06 Å. The fifth Cu-O distance, involving the O_{Eq} atom opposite the vacancy site, increases by 0.07 Å. In this configuration the Bader charge on the dopant is 9.7 electrons and the spin magnetization is 0.75 μ_B, indicating a Cu^{2+} oxidation state.

For the formation of a second, reducing oxygen vacancy, the most stable site is a second equatorial site neighboring the dopant and adjacent to the first vacancy. This oxygen vacancy forms with an energy cost of +3.27 eV and the local geometry about the dopant is shown in the bottom panels of Figure 2, with the oxygen vacancies indicated by black circles. This energy cost is similar to undoped bulk anatase so that Cu doping has no significant effect on the reducibility of anatase.

Both Cu-O_{Ap} distances contract to 1.93 Å, while the two remaining Cu-O_{Eq} distances are 2.08 Å and 2.10 Å. After formation of the second oxygen vacancy two electrons are released and we analyze computed Bader charges and spin magnetizations to determine where these electrons are localized. For the Cu dopant the Bader charge increases from 9.7 to 10.3 electrons and the spin magnetization is 0 μ_B, consistent with reduction from Cu^{2+} to Cu^{+}. The second electron localizes at a Ti site which is five-fold-coordinated due to formation of the second oxygen vacancy. This site has a Bader charge of 1.7 electrons and a spin magnetization of 0.95 μ_B, indicating reduction to Ti^{3+}. For comparison, the Ti^{4+} ions in TiO_2 have computed Bader charges of 1.29–1.34 electrons.

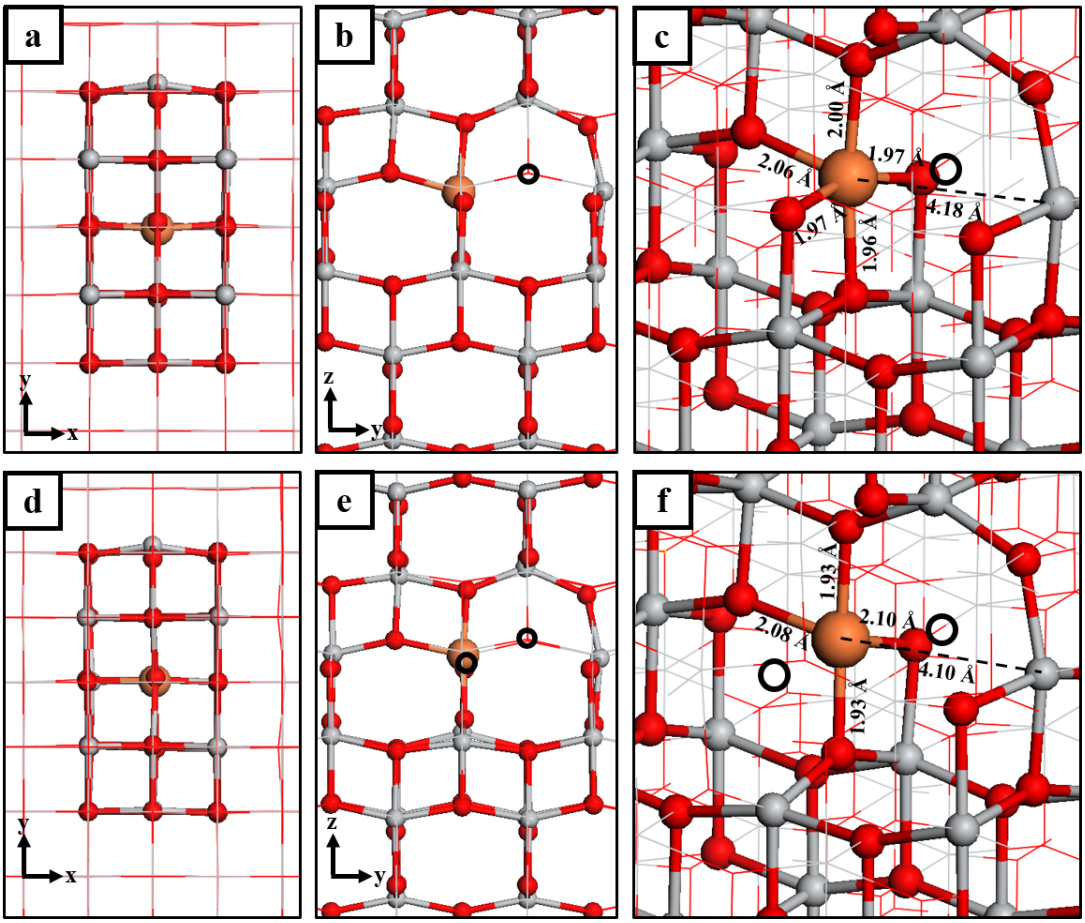


Figure 2. Atomic structure of Cu-doped anatase TiO_2 after formation of a charge compensating oxygen vacancy (top panels) and after formation of a second, reducing oxygen vacancy (bottom panels). Panels (**a**,**d**) xy-plane geometry; (**b**,**e**) yz-plane geometry; (**c**,**f**) lattice distortions around the dopant site. The black circles represent the O vacancy sites.

The projected electronic density of states (PEDOS) plots for pure TiO_2 anatase is shown in Figure 3a, highlighting the typical O 2p dominated valance band region and the Ti 3d dominated conduction band region. Figure 3b shows the PEDOS for Cu doping where a clear Cu^{2+} derived state is present in the TiO_2 energy gap.

For the ground state of Cu-doped anatase, with a single, compensating oxygen vacancy, and the reduced system, with two oxygen vacancies, the PEDOS are shown in the bottom panels of Figure 3. For the ground state system (Figure 3c) the empty 3d state of the Cu^{2+} ion lies above the conduction band minimum (CBM) of the TiO_2 host, so that the dopant has no impact on the magnitude of the band gap. However, states emerge in the band gap after formation of the second oxygen vacancy, as shown in Figure 3d. These states are derived from the reduced Ti^{3+} and Cu^{+} ions which may act as recombination

centers, thereby reducing photocatalytic activity. In the reduced system, Cu-derived states also emerge at the valence band edge and extend the VBM to higher energies leading to a decrease in the band gap.

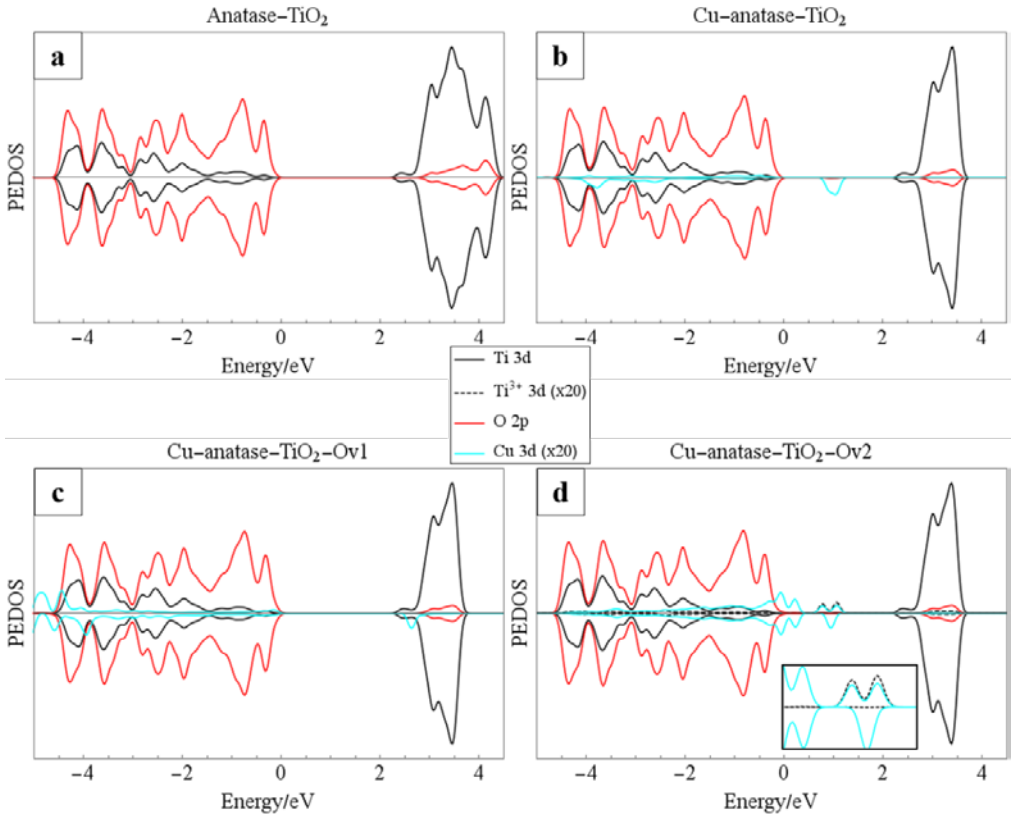


Figure 3. Projected electronic density of states (PEDOS) plots for (**a**) undoped anatase, (**b**) Cu-doped anatase with no oxygen vacancies and (**c**) after formation of a single, charge compensating oxygen vacancy and (**d**) after formation of a second, reducing oxygen vacancy.

3.2. X-ray Diffraction (XRD)

XRD is utilized to study the impact of Cu doping on the anatase to rutile phase transition of TiO_2 at various calcination temperatures. Figure 4a shows the XRD profiles of pure anatase TiO_2 and 0.5% Cu-TiO_2 (calcined at 500 °C, 600 °C, 650 °C and 700 °C). XRD spectrum of rutile TiO_2 is also provided for reference. The spectra of undoped samples of TiO_2 for all the given temperatures are given in Figure S1. The anatase and rutile peak intensities are generally observed at 25.4° and 27.3°, respectively, (101 and 110) [15]. These values were used to calculate the percentage of anatase and rutile of TiO_2 in all samples using the Spurr equation (Equation (2)). Cu-TiO_2 at 500 °C and 600 °C exhibited 100% of anatase while the sample at 700 °C showed 100% of rutile. Interestingly, calcined at 650 °C yielded a mixture phase constituting 55% of anatase and 45% of rutile TiO_2 (Figure 4b).

The diffractogram also illustrates the increase in the intensity of the signature peaks of both anatase and rutile phases with increase in calcination temperature. The Schrerr equation (Equation (3)) is used to calculate the average crystalline size (Table 1). The decrease in the FWHM values helped in exhibiting the increase in average crystallite size from 8.83 nm for anatase TiO_2 to 28.8 nm for the mixed phase sample (calcined at 650 °C). This is attributed to the thermally promoted crystallite growth [70]. For any photocatalytic application the need for improved visible light activity and high temperature stability are two fundamental desirable properties. In this study, the XRD results shows the presence of mixed phase at a high calcination temperature of 650 °C by doping a very minute fraction of Cu. This prime reason makes the sample an interesting candidate for further studies and hence, hereafter, the mixed phase sample was used for further characterizations and application. Additionally, anatase (TiO_2—500 °C) and rutile (TiO_2—700 °C) samples are taken as controls.

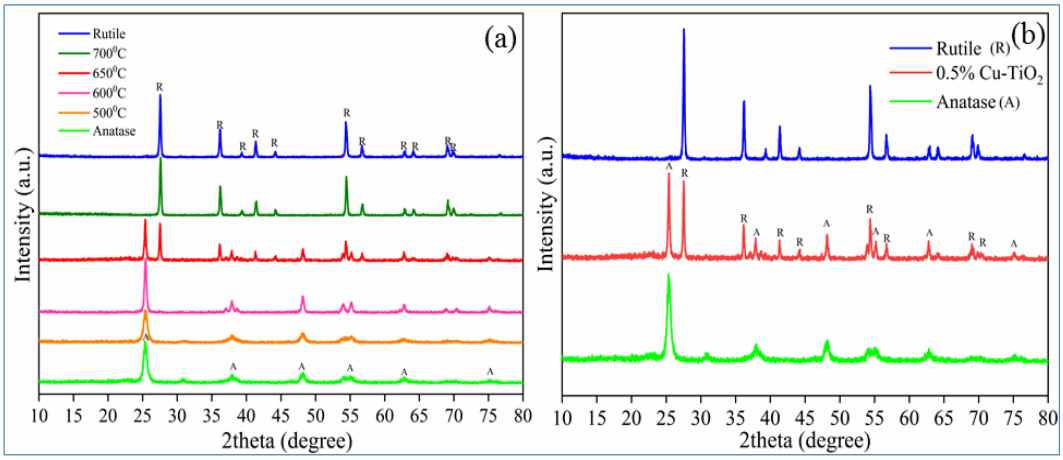


Figure 4. (**a**) XRD profiles of pure anatase TiO_2, pure rutile TiO_2, Cu-TiO_2 samples (calcined at 500 °C, 600 °C, 650 °C and 700 °C) and (**b**) XRD profiles of pure anatase TiO_2, pure rutile TiO_2 and the Cu-TiO_2 calcined at 650 °C.

Table 1. The average particle size of samples calcined at various calcination temperatures.

Sample	Calcined Temperature (in °C)	Particle Size (in nm)
Control●	500	8.83
0.5% Cu-TiO_2	500	11.34
0.5% Cu-TiO_2	600	22.35
0.5% Cu-TiO_2	650	28.84
0.5% Cu-TiO_2	700	32.93
Control●	700	33.80

●—pure TiO_2 anatase; ●—pure TiO_2 rutile.

3.3. Raman Spectroscopy

The anatase-to-rutile transition of Cu-TiO_2 was further examined using Raman spectroscopy. A typical Raman spectrum shows characteristic modes at different wavenumbers, corresponding to Raman shifts. The active modes for anatase are A_{1g}, $2B_{1g}$ and $3E_g$ at 147, 197, 396, 516 and 638 cm^{-1} respectively. For rutile, the Raman active modes are A_{1g}, B_{1g}, B_{2g} and $3E_g$ at 144, 238, 446 and 612 cm^{-1} [15]. Raman spectra displayed the presence of the titania peaks and did not exhibit the occurrence of copper/copper oxides or other impurities (Figure 5). The Raman results are consistent with the data observed in XRD analysis. The anatase phase of titania is retained well by the Cu doping. Similar results were also observed for higher concentration (<0.5 mol %) of Cu-doped samples [71–73]. However, as observed in the figure below, the doped sample shows a small decrease in frequency of 2.35 cm^{-1} (red shift as illustrated in the inset of the image). Decrease in frequency is the resultant of the Cu insertion in the TiO_2 lattice, which subsequently weakens the bond between the O-Ti-O bond, therefore leading to a higher lattice constant.

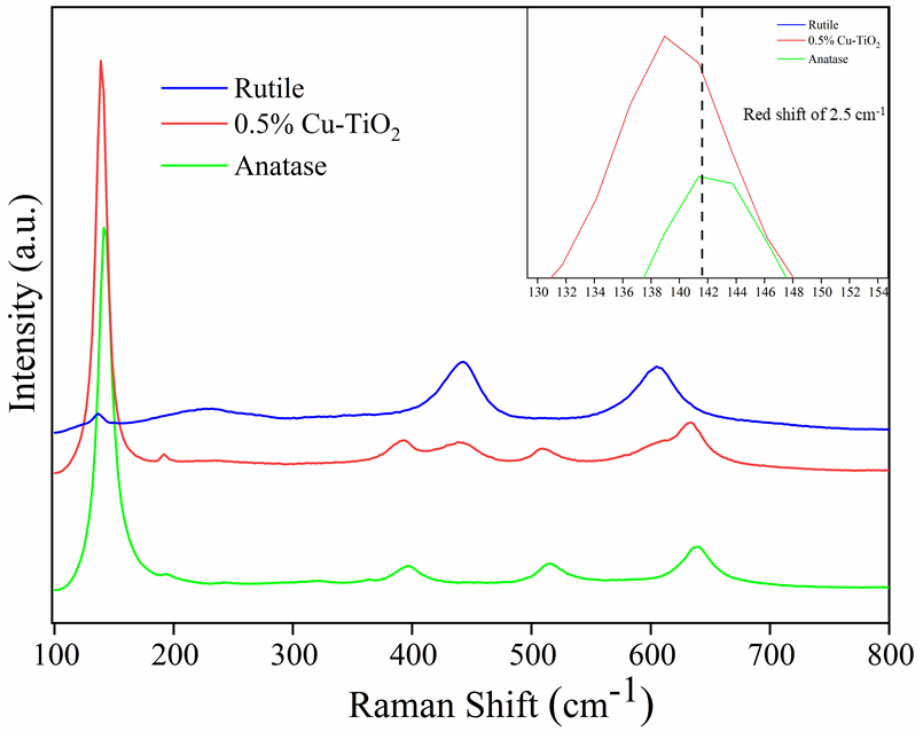


Figure 5. Raman spectra of anatase, rutile and 0.5% Cu-TiO_2 650 °C.

3.4. X-ray Photoelectron Spectroscopy (XPS)

The X-ray Photoelectron Spectroscopy (XPS) quantifications were performed to analyze the elemental composition of anatase TiO_2 and Cu-doped samples. Figure 6a provides the survey spectrum of anatase TiO_2 and 0.5% Cu-doped TiO_2 calcined at 650 °C. It illustrates the presence of titanium, oxygen and additionally copper for the doped sample. A small amount of carbon peak also emerged, which is acquired during the synthesis and calcination processes. An introduction of Cu into TiO_2 lattice resulted in substitution of Ti^{4+} by the Cu^{2+} ion [74]. Hence, instead of O-Ti-O bonds new bonds of Cu-O are established. Figure 6b provides the high-resolution spectra of Ti 2p, which exhibits very sharp, symmetric and intense peaks, indicating the presence of Ti^{+4} state. The deconvoluted Ti 2p peaks of anatase appears at 457.4 eV and 463.06 eV, which is ascribed to Ti $2p_{3/2}$ and Ti $2p_{1/2}$ (Ti-O bond) respectively. In the case of Cu-TiO_2 650 °C, a significant shift of around 1.7 eV is observed for both Ti $2p_{3/2}$ and Ti $2p_{1/2}$ (459.06 eV and 464.83 eV) [75,76]. The shift in the peak is attributed to the introduction of Cu in the lattice. The Ti 2p peaks of Cu-TiO_2 650 °C do not show any indication of Ti^{3+} or Ti^{2+} states. Similarly, Figure 6c illustrates the high-resolution spectra of O 1s, where peaks at 528.59 eV constitutes to the crystal lattice oxygen (O-Ti^{4+}) and 530.40 eV for adsorbed hydroxyl or oxygen molecules. Whilst the O 1s spectrum of the doped sample showed a similar shift as observed for Ti 2p spectrum attributed to the introduction of copper atom in the lattice [77]. The Cu $2p^3$ spectrum (Figure 6d) on deconvolution exhibits an intense peak at 933.13 eV and a shorter peak at 934.60 eV, ascribed to Cu^{+} and Cu^{2+} states [75].

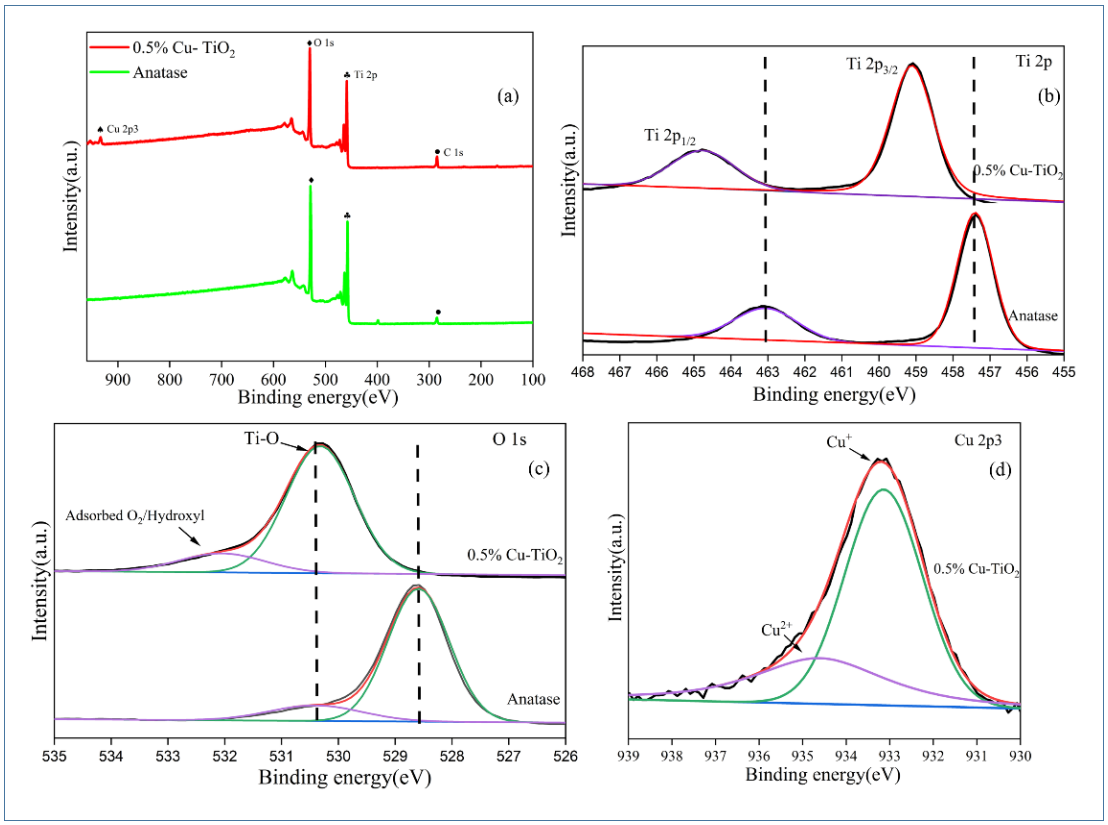


Figure 6. (**a**) Survey spectrum of anatase and 0.5% Cu-TiO_2; (**b**) high resolution Ti 2p spectra of anatase and 0.5% Cu-TiO_2 650 °C.; (**c**) high resolution O 1s spectra of anatase and 0.5% Cu-TiO_2 650 °C.; (**d**) high resolution Cu 2p3 spectra of 0.5% Cu-TiO_2 650 °C.

Figure 7 illustrates the high-resolution spectra of 0.5% Cu-TiO_2 samples calcined at different temperatures. It is observed that with increase in temperature from 500 °C to 700 °C the Cu^+ state observed at 933.1 eV gradually decreases. While the Cu^{2+} state at 934.3 eV is only observed at 650 °C and 700 °C. Additionally, two satellite peaks of Cu^{2+} were also observed at 941.3 eV and 944.2 eV for 700 °C [75,78]. The intensity of the peak at 934.3 eV gradually increases with the increase in calcination temperature [75,79]. Usually, the TiO_2 exhibits stable anatase phase in the range of 500–600 °C and converts to rutile with increase in temperature. However, the change in oxidation states with increase in calcination temperature in our Cu-doped samples (change in oxygen vacancies) contributes to the high temperature stability of the oxygen-rich anatase phase at 650 °C [23,34].

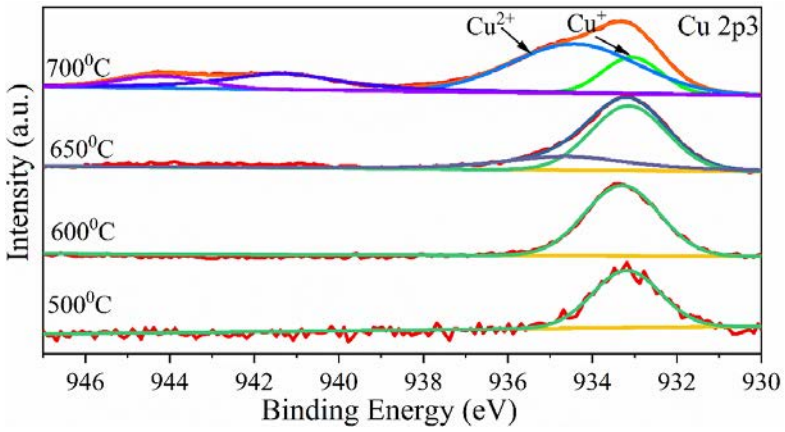


Figure 7. High-resolution Cu 2p3 spectra of 0.5% Cu-TiO_2 samples calcined at different temperatures.

Previous studies have reported that Cu^{2+}/Cu^{+} replaces Ti^{4+} from the TiO_2 lattice resulting in the formation of oxygen vacancies. This leads to the formation of high absorption of a visible light and narrowing of band gap, as observed in Figure 8. The TiO_6 octahedron has Ti in Ti^{4+} state with an ionic radius of 0.0605 nm. On the other hand, the ionic radii of Cu^{2+} and Cu^{+} exist as 0.073 nm and 0.077 nm, respectively [80]. Moreover, the electronegativity values of Ti and Cu are 1.54 and 1.90, respectively. According to Hume-Rothery principles, the lattice substitution between atoms could only happen if the differences between them is less than 20% [77]. Considering the difference in the values of ionic radii and the electronegativity of the atoms, the substitution process of Ti by Cu would be challenging. Early DFT-based theoretical studies have reported that maximum doping concentration for Cu should be less than 0.3 at % to cause a lattice substitution [81]. Thus, in the present study a doping of 0.5 mol % exhibits the successful doping of Cu inside the TiO_2 lattice. The doped copper existing in both oxidation states (Cu^{+} and Cu^{2+}) results in the formation of single and double oxygen vacancies. However, the Ti 2p and O 1s spectra fail to provide any information regarding the new vacancies formed in the doped sample. The presence of adsorbed O_2 and hydroxyl molecules is indicated in the O 1s spectra, which explains the occupancy of the adsorbed molecules at the vacancy sites.

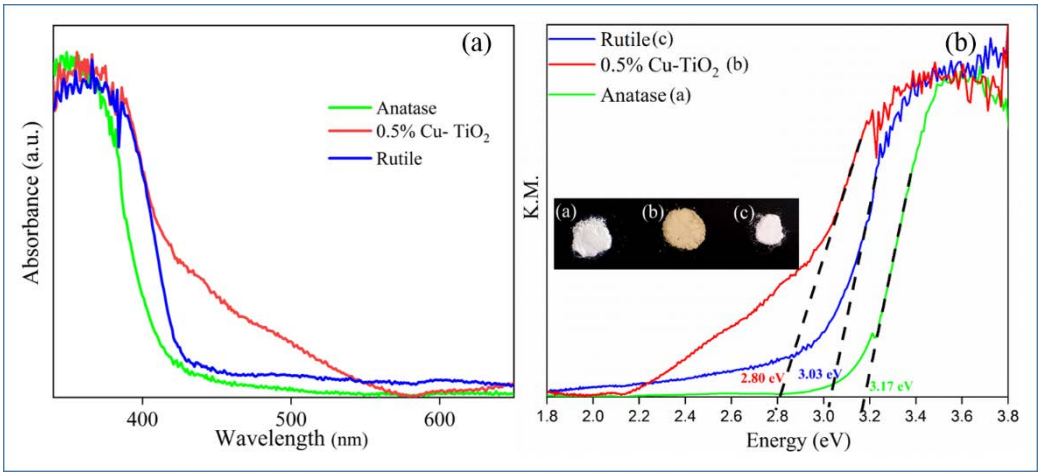


Figure 8. (**a**) UV–Vis absorption spectra and (**b**) Tauc plots of anatase (control), rutile (control) and 0.5% Cu-TiO_2 650 °C.

3.5. UV–Vis Absorption and Bandgap Estimation

The electronic band structures of the as-prepared samples were analyzed by UV–Vis absorption (Figure 8). The pristine TiO_2 at anatase phase shows an intense absorption in the Ultra-Violet region (around 350 nm). While the rutile sample exhibits at 380 nm, on the other hand the Cu-doped sample indicated a red shift extending up to 600 nm. This is attributed to the characteristic surface plasmon resonance of Cu nanoparticles. The successful doping of Cu is also evident from the change in the color observed in the samples, shifting from pure white to light yellow (as shown in the inset of Figure 8b). The band gap value of the samples was estimated using the Kubelka–Munk equation (Equation (4)) [51]. The band gap values of pristine TiO_2 at anatase and rutile phases were observed to be 3.17 eV and 3.03 eV, respectively. The Cu-doped sample showed a significant dip in the band gap value up to 2.8 eV.

3.6. Photocatalytic Antibacterial Activity

To demonstrate the visible light efficiency of the doped Cu samples, photocatalytic antibacterial experiments were carried out under dark and visible light irradiation, respectively. The following data was also compared with the pristine TiO_2 in anatase and rutile phases (Figure 9). The samples were evaluated in relation to two different bacterial strains (*E. coli* and *S. aureus*). In the absence of

photocatalyst, the growth of both the strains persisted under light and dark conditions. On the other hand, on exposing the bacterial cells with catalyst (1 g/L) under visible light and dark conditions yielded different results.

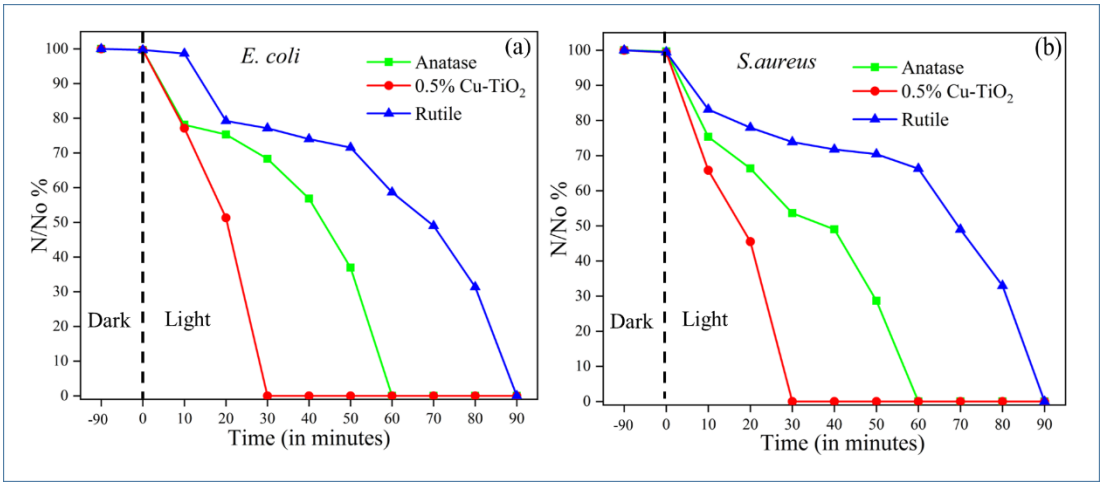


Figure 9. Photocatalytic inactivation of (**a**) *E. coli* and (**b**) *S. aureus* with anatase, rutile and 0.5% Cu-TiO_2 650 °C samples.

In dark atmosphere, no significant change in bacterial growth was observed even after 90 min. While the bacterial growth significantly decreased within 30 min of visible light irradiation (5-Log reduction shown in Figure 10); 99.9999% bacterial reduction was achieved in the presence of Cu-doped samples in a time span as short as 30 min (Figure 11). Moreover, the anatase and rutile TiO_2 samples showed complete disinfection within 60 and 90 min of irradiation respectively. This indicates the stability of the cell structure and the importance of light in the inactivation process.

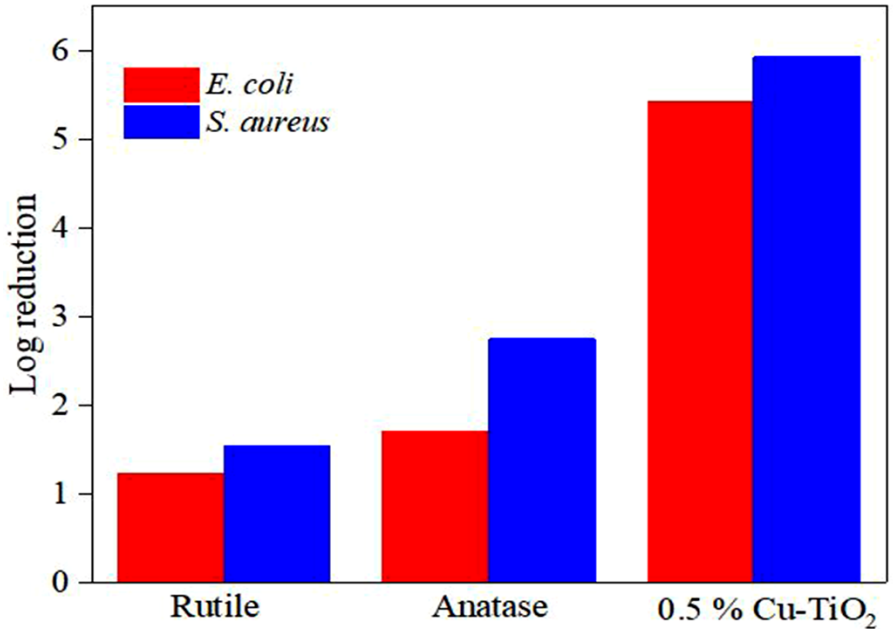


Figure 10. Photocatalytic antibacterial disinfection efficiency of anatase, rutile and 0.5% Cu-TiO_2 samples with *E. coli* and *S. aureus*.

However, the inactivation observed is a synergetic effect of TiO_2, as well as Cu ions in the presence of visible light. None of the test samples in a dark atmosphere exhibited any bactericidal property. Therefore, the cease in cell proliferation is a photo-induced inactivation rather than chemo-toxic killing

of bacterial cells. The introduction of Cu significantly improved the visible absorption efficiency which effectively contributed to the enhanced bacterial inactivation kinetics as observed compared to the control samples.

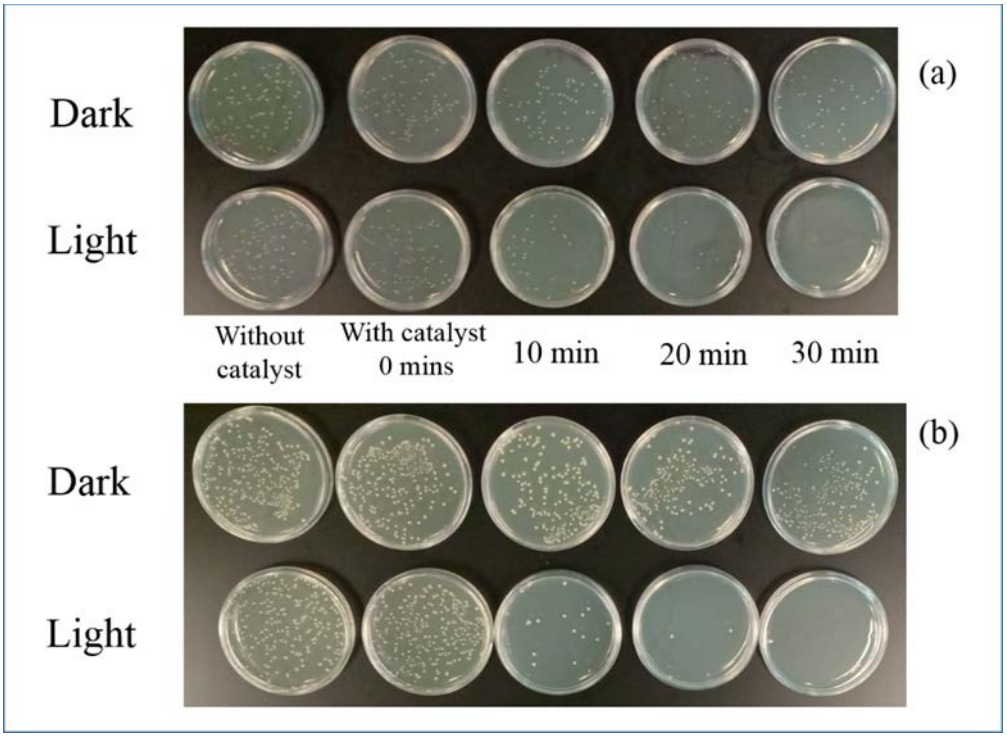


Figure 11. Images of (**a**) *E. coli* colonies and (**b**) *S. aureus* colonies on agar plates after various time intervals of Cu-TiO_2 650 °C.

4. Discussion

From the DFT analysis, it is assumed that the creation of a single vacancy by Cu in Cu^{2+} (CuO) state only exists on the surface which does not contributes to the alteration of the band gap of the material at a very small mole percentage. On the other hand, dual vacancy created by the Cu dopant (Cu^{+} state) does change the band gap of the material, as well as introducing various trap sites in between. This reduces the overall band gap energy, but the trap sites potentially serve as recombination centers. XPS analysis showed the co-existence of Cu in +1 (Cu_2O) and +2 (CuO) oxidation states, where Cu^{+} is the major species in the sample which necessarily committed in the variation of optical property of the sample which is also evident in the UV–vis absorption plot (Figure 8a). A possible photocatalytic disinfection mechanism is proposed based on the DFT, XPS and UV–vis results (Figure 12).

On light illumination, electron-hole pairs are generated on the individual surfaces of TiO_2 and Cu_2O. The photo-excited charge carriers have the ability to recombine or participate in the photocatalysis reaction. TiO_2 (a n-type semiconductor) has the conduction and valence band edge values at 3.1 eV and −0.1 eV, respectively [25], while the Cu_2O (a p-type semiconductor) has the conduction and valence band edge potential at 1.91 eV and −0.26 eV, respectively [82]. Under light irradiation, both semiconductor surfaces are in contact, drives the electron transfer process (Figure 12a). As the electron from conduction band of Cu_2O moves to that of TiO_2 and the hole migrates from the valence band of TiO_2 to that of Cu_2O [83]. This results in the lowering of the Fermi level of Cu_2O and rising of the TiO_2, such that to reach a pseudo equilibrium phase resulting in formation of internal electric field. Furthermore, this external field prevents the flow of charge carriers from the opposite sites and thus makes these charge carriers participate in the photocatalytic reaction. Apart from the p-n junction formed by the Cu_2O and anatase TiO_2, there exists a considerable proportion of rutile phase in our samples. This anatase and rutile mixture forms a possible type 2 heterojunction which also

necessarily contributes to the improved catalytic activity (Figure 12b) [84]. The enhanced antimicrobial activity could also be attributed to the well-known bactericide activity of Cu ions in the sample [85].

The charge carriers formed on various heterojunction sites (type 2 junction of anatase–rutile and p-n junction of Cu_2O-anatase TiO_2) reacts with the oxygen and water adsorbed on the catalyst surface to produce superoxide radicals and hydroxyl radicals, respectively. These reactive oxygen species (ROS) further interact with the bacterial cell wall which results in membrane disruption and outflow of intracellular materials; this results in cell lysis (Figure 12). In addition to this, the ROS produced has the ability to interact with the sugar phosphate groups present in the DNA of the bacteria to cause gene alteration. Furthermore, altering the protein expression responsible for cellular functioning leads to additional cell damage [11,86].

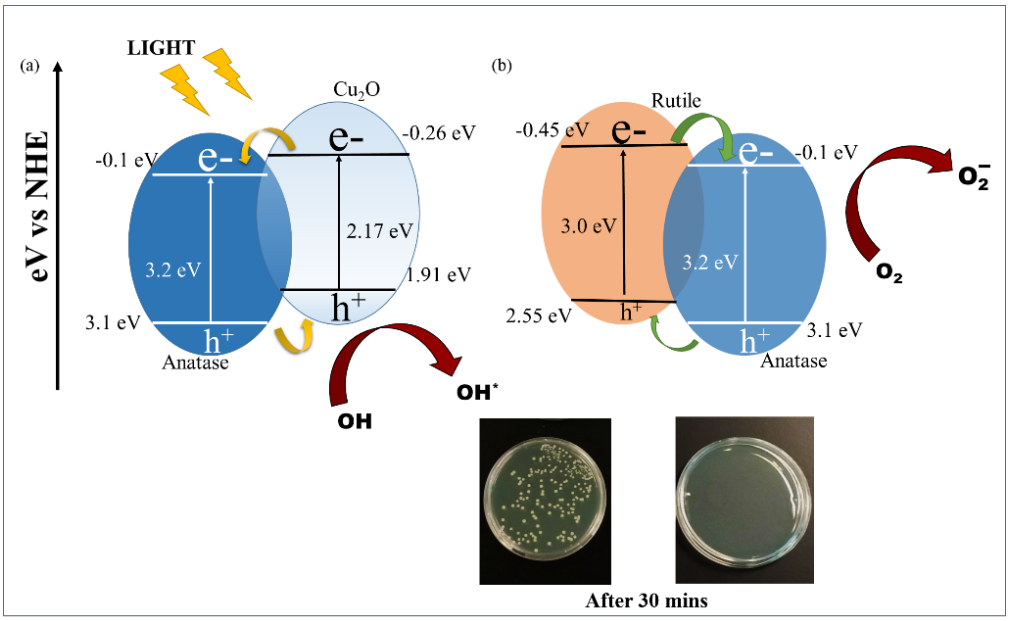


Figure 12. Schematic illustration of photocatalytic disinfection shown by possible two mechanisms (**a**) p-n junction by Cu_2O and TiO_2 (**b**) Type-2 heterostructure by anatase and rutile titania.

5. Conclusions

In the present work, a 0.5 mol % Cu-doped TiO_2 visible light active semiconductor material has been synthesized through a sol-gel approach. The as-synthesized materials have been thoroughly characterized with the help of XRD, XPS, Raman, UV–DRS and DFT analyses. The introduction of a small mole percent of Cu inside the TiO_2 crystal lattice has led to increased thermal stability and antimicrobial efficiency. The anatase phase of TiO_2 is retained well up to 650 °C by Cu doping. Almost all micro-organisms tested (*E. coli* and *S. aureus*) are inactivated by Cu-TiO_2 within 30 min of visible light irradiation. The high antimicrobial efficiency of Cu-TiO_2 is attributed to the synergistic effect of p-n junction (between TiO_2 anatase and rutile), heterojunctions formed (between TiO_2 and Cu_2O) and of copper ions. The results have also compared with pure TiO_2 anatase and rutile. The as-synthesized high temperature stable smart materials could be used to develop antimicrobial coatings or can be incorporated in paints or building wares (ceramics, tiles, etc.) as a potential antibacterial agent.

Supplementary Materials: The following are available online at http://www.mdpi.com/2076-3417/8/11/2067/s1, Figure S1: XRD profiles of undoped TiO_2 at different temperatures, Table S1: Summarise glance of literature of Cu-TiO_2 for Antimicrobial disinfection.

Author Contributions: Conceptualization, S.C.P.; methodology design, C.B.; experimental, investigation, data creation, data analysis and draft preparation S.M. and P.G.; data creation and editing, S.R., M.N., S.J.H.; editing, V.K., C.B. and S.C.P.; supervision, J.B. and S.C.P.

Funding: The research was funded by European Union's INTERREG VA Programme, managed by the Special EU Programmes Body (SEUPB), with match funding provided by the Department for the Economy and Department of Jobs, Enterprise and Innovation in Dublin, Ireland, grand number IVA5033. P.G & C.B would like to acknowledge the Institute of Technology Sligo President's Bursary for providing financial support, grant number PPRES052 and PPRES032. S.R. and M.N. acknowledge support from Science Foundation Ireland through the US-Ireland R&D Parntershop program, Grant number SFI/US/14/e2915 and the ERA.Net for Materials Research and Innovation (M-ERA.Net 2), Horizon 2020 grant agreement number 685451, SFI Grant Number SFI/16/M-ERA/3418 (RATOCAT).

Acknowledgments: S.M., P.G., C.B. and S.C.P. would like to acknowledge access to Raman Spectroscopy at Centre for Research in Engineering Surface Technology (CREST), FOCAS Institute, Dublin Institute of Technology, Kevin Street, Dublin, Ireland. S.M. & P.G. would like to acknowledge Saoirse Dervin for helping in bacterial culture. S.R. and M.N. acknowledge access to SFI funded computing resources at Tyndall Institute and the SFI/HEA funded Irish Centre for High End Computing. We are grateful for support from the COST Action CM1104 "Reducible Metal Oxides, Structure and Function".

Conflicts of Interest: The authors declare no conflict of interest.

References

1. Heseltine, E.; Rosen, J. *WHO Guidelines for Indoor Air Quality: Dampness and Mould*; WHO Regional Office Europe: København, Denmark, 2009.
2. Jones, A.P. Indoor air quality and health. *Atmos. Environ.* **1999**, *33*, 4535–4564. [CrossRef]
3. Burger, H. Bioaerosols: Prevalence and health effects in the indoor environment. *J. Allergy Clin. Immunol.* **1990**, *86*, 687–701. [CrossRef]
4. Robbins, C.A.; Swenson, L.J.; Nealley, M.L.; Kelman, B.J.; Gots, R.E. Health effects of mycotoxins in indoor air: A critical review. *Appl. Occup. Environ. Hyg.* **2000**, *15*, 773–784. [CrossRef] [PubMed]
5. Verdier, T.; Coutand, M.; Bertron, A.; Roques, C. A review of indoor microbial growth across building materials and sampling and analysis methods. *Build. Environ.* **2014**, *80*, 136–149. [CrossRef]
6. Dillon, H.K.; Miller, J.D.; Sorenson, W.; Douwes, J.; Jacobs, R.R. Review of methods applicable to the assessment of mold exposure to children. *Environ. Health Perspect.* **1999**, *107* (Suppl. 3), 473. [CrossRef] [PubMed]
7. Redlich, C.A.; Sparer, J.; Cullen, M.R. Sick-building syndrome. *Lancet* **1997**, *349*, 1013–1016. [CrossRef]
8. Pacheco-Torgal, F.; Jalali, S. Nanotechnology: Advantages and drawbacks in the field of construction and building materials. *Constr. Build. Mater.* **2011**, *25*, 582–590. [CrossRef]
9. Huang, Y.; Ho, S.S.H.; Lu, Y.; Niu, R.; Xu, L.; Cao, J.; Lee, S. Removal of indoor volatile organic compounds via photocatalytic oxidation: A short review and prospect. *Molecules* **2016**, *21*, 56. [CrossRef] [PubMed]
10. Byrne, C.; Subramanian, G.; Pillai, S.C. Recent advances in photocatalysis for environmental applications. *J. Environ. Chem. Eng.* **2018**, *6*, 3531–3555. [CrossRef]
11. Verdier, T.; Coutand, M.; Bertron, A.; Roques, C. Antibacterial activity of TiO_2 photocatalyst alone or in coatings on *E. coli*: The influence of methodological aspects. *Coatings* **2014**, *4*, 670–686. [CrossRef]
12. Etacheri, V.; Di Valentin, C.; Schneider, J.; Bahnemann, D.; Pillai, S.C. Visible-light activation of TiO_2 photocatalysts: Advances in theory and experiments. *J. Photochem. Photobiol. C* **2015**, *25*, 1–29. [CrossRef]
13. Pillai, S.C.; Periyat, P.; George, R.; McCormack, D.E.; Seery, M.K.; Hayden, H.; Colreavy, J.; Corr, D.; Hinder, S.J. Synthesis of high-temperature stable anatase TiO_2 photocatalyst. *J. Phys. Chem. C* **2007**, *111*, 1605–1611. [CrossRef]
14. Banerjee, S.; Pillai, S.C.; Falaras, P.; O'shea, K.E.; Byrne, J.A.; Dionysiou, D.D. New insights into the mechanism of visible light photocatalysis. *J. Phys. Chem. Lett.* **2014**, *5*, 2543–2554. [CrossRef] [PubMed]
15. Byrne, C.; Fagan, R.; Hinder, S.; McCormack, D.E.; Pillai, S.C. New approach of modifying the anatase to rutile transition temperature in TiO_2 photocatalysts. *RSC Adv.* **2016**, *6*, 95232–95238. [CrossRef]
16. Periyat, P.; Baiju, K.; Mukundan, P.; Pillai, P.; Warrier, K. High temperature stable mesoporous anatase TiO_2 photocatalyst achieved by silica addition. *Appl. Catal. A* **2008**, *349*, 13–19. [CrossRef]
17. Panneri, S.; Ganguly, P.; Nair, B.N.; Mohamed, A.A.P.; Warrier, K.G.K.; Hareesh, U.N.S. Role of precursors on the photophysical properties of carbon nitride and its application for antibiotic degradation. *Environ. Sci. Pollut. Res.* **2017**, *24*, 8609–8618. [CrossRef] [PubMed]

18. Vignesh, K.; Suganthi, A.; Min, B.-K.; Kang, M. Photocatalytic activity of magnetically recoverable $MnFe_2O_4$/g-C_3N_4/TiO_2 nanocomposite under simulated solar light irradiation. *J. Mol. Catal. A* **2014**, *395*, 373–383. [CrossRef]
19. Vignesh, K.; Priyanka, R.; Hariharan, R.; Rajarajan, M.; Suganthi, A. Fabrication of CdS and $CuWO_4$ modified TiO_2 nanoparticles and its photocatalytic activity under visible light irradiation. *J. Ind. Eng. Chem.* **2014**, *20*, 435–443. [CrossRef]
20. Hanaor, D.A.H.; Sorrell, C.C. Review of the anatase to rutile phase transformation. *J. Mater. Sci.* **2011**, *46*, 855–874. [CrossRef]
21. El-Sheikh, S.M.; Zhang, G.; El-Hosainy, H.M.; Ismail, A.A.; O'Shea, K.E.; Falaras, P.; Kontos, A.G.; Dionysiou, D.D. High performance sulfur, nitrogen and carbon doped mesoporous anatase–brookite TiO_2 photocatalyst for the removal of microcystin-LR under visible light irradiation. *J. Hazard. Mater.* **2014**, *280*, 723–733. [CrossRef] [PubMed]
22. Etacheri, V.; Seery, M.K.; Hinder, S.J.; Pillai, S.C. Nanostructured Ti_{1-x} $S_xO_{2-y}N_y$ Heterojunctions for Efficient Visible-Light-Induced Photocatalysis. *Inorg. Chem.* **2012**, *51*, 7164–7173. [CrossRef] [PubMed]
23. Etacheri, V.; Seery, M.K.; Hinder, S.J.; Pillai, S.C. Oxygen rich titania: A dopant free, high temperature stable, and visible-light active anatase photocatalyst. *Adv. Funct. Mater.* **2011**, *21*, 3744–3752. [CrossRef]
24. Seery, M.K.; George, R.; Floris, P.; Pillai, S.C. Silver doped titanium dioxide nanomaterials for enhanced visible light photocatalysis. *J. Photochem. Photobiol. A* **2007**, *189*, 258–263. [CrossRef]
25. Yoong, L.; Chong, F.K.; Dutta, B.K. Development of copper-doped TiO_2 photocatalyst for hydrogen production under visible light. *Energy* **2009**, *34*, 1652–1661. [CrossRef]
26. Xu, S.; Du, A.J.; Liu, J.; Ng, J.; Sun, D.D. Highly efficient CuO incorporated TiO_2 nanotube photocatalyst for hydrogen production from water. *Int. J. Hydrogen Energy* **2011**, *36*, 6560–6568. [CrossRef]
27. Lalitha, K.; Sadanandam, G.; Kumari, V.D.; Subrahmanyam, M.; Sreedhar, B.; Hebalkar, N.Y. Highly stabilized and finely dispersed Cu_2O/TiO_2: A promising visible sensitive photocatalyst for continuous production of hydrogen from glycerol: Water mixtures. *J. Phys. Chem. C* **2010**, *114*, 22181–22189. [CrossRef]
28. Wu, F.; Hu, X.; Fan, J.; Liu, E.; Sun, T.; Kang, L.; Hou, W.; Zhu, C.; Liu, H. Photocatalytic activity of Ag/TiO_2 nanotube arrays enhanced by surface plasmon resonance and application in hydrogen evolution by water splitting. *Plasmonics* **2013**, *8*, 501–508. [CrossRef]
29. Nasution, H.W.; Purnama, E.; Kosela, S.; Gunlazuardi, J. Photocatalytic reduction of CO_2 on copper-doped Titania catalysts prepared by improved-impregnation method. *Catal. Commun.* **2005**, *6*, 313–319. [CrossRef]
30. Kim, T.W.; Ha, H.-W.; Paek, M.-J.; Hyun, S.-H.; Choy, J.-H.; Hwang, S.-J. Unique phase transformation behavior and visible light photocatalytic activity of titanium oxide hybridized with copper oxide. *J. Mater. Chem.* **2010**, *20*, 3238–3245. [CrossRef]
31. Varghese, O.K.; Paulose, M.; LaTempa, T.J.; Grimes, C.A. High-rate solar photocatalytic conversion of CO_2 and water vapor to hydrocarbon fuels. *Nano Lett.* **2009**, *9*, 731–737. [CrossRef] [PubMed]
32. Colon, G.; Maicu, M.; Hidalgo, M.S.; Navio, J. Cu-doped TiO_2 systems with improved photocatalytic activity. *Appl. Catal. B* **2006**, *67*, 41–51. [CrossRef]
33. Hassan, M.S.; Amna, T.; Kim, H.Y.; Khil, M.-S. Enhanced bactericidal effect of novel CuO/TiO_2 composite nanorods and a mechanism thereof. *Compos. Part B* **2013**, *45*, 904–910. [CrossRef]
34. Sunada, K.; Watanabe, T.; Hashimoto, K. Bactericidal activity of copper-deposited TiO_2 thin film under weak UV light illumination. *Environ. Sci. Technol.* **2003**, *37*, 4785–4789. [CrossRef] [PubMed]
35. Yousef, A.; El-Halwany, M.; Barakat, N.A.; Al-Maghrabi, M.N.; Kim, H.Y. Cu0-doped TiO_2 nanofibers as potential photocatalyst and antimicrobial agent. *J. Ind. Eng. Chem.* **2015**, *26*, 251–258. [CrossRef]
36. Karunakaran, C.; Abiramasundari, G.; Gomathisankar, P.; Manikandan, G.; Anandi, V. Cu-doped TiO_2 nanoparticles for photocatalytic disinfection of bacteria under visible light. *J. Colloid Interface Sci.* **2010**, *352*, 68–74. [CrossRef] [PubMed]
37. Leyland, N.S.; Podporska-Carroll, J.; Browne, J.; Hinder, S.J.; Quilty, B.; Pillai, S.C. Highly Efficient F, Cu doped TiO_2 anti-bacterial visible light active photocatalytic coatings to combat hospital-acquired infections. *Sci. Rep.* **2016**, *6*, 24770. [CrossRef] [PubMed]
38. Yadav, H.M.; Otari, S.V.; Koli, V.B.; Mali, S.S.; Hong, C.K.; Pawar, S.H.; Delekar, S.D. Preparation and characterization of copper-doped anatase TiO_2 nanoparticles with visible light photocatalytic antibacterial activity. *J. Photochem. Photobiol. A* **2014**, *280*, 32–38. [CrossRef]

39. Miao, Y.; Xu, X.; Liu, K.; Wang, N. Preparation of novel Cu/TiO_2 mischcrystal composites and antibacterial activities for *Escherichia coli* under visible light. *Ceram. Int.* **2017**, *43*, 9658–9663. [CrossRef]
40. Ohwaki, T.; Saeki, S.; Aoki, K.; Morikawa, T. Evaluation of photocatalytic activities and characteristics of Cu-or Fe-modified nitrogen-doped titanium dioxides for applications in environmental purification. *Jpn. J. Appl. Phys.* **2015**, *55*, 01AA05. [CrossRef]
41. Kresse, G.; Furthmüller, J. Efficiency of ab-initio total energy calculations for metals and semiconductors using a plane-wave basis set. *Comput. Mater. Sci.* **1996**, *6*, 15–50. [CrossRef]
42. Kresse, G.; Furthmüller, J. Efficient iterative schemes for ab initio total-energy calculations using a plane-wave basis set. *Phys. Rev. B* **1996**, *54*, 11169. [CrossRef]
43. Kresse, G.; Joubert, D. From ultrasoft pseudopotentials to the projector augmented-wave method. *Phys. Rev. B* **1999**, *59*, 1758–1775. [CrossRef]
44. Blöchl, P.E. Projector augmented-wave method. *Phys. Rev. B* **1994**, *50*, 17953–17979. [CrossRef]
45. Chand, R.; Obuchi, E.; Katoh, K.; Luitel, H.N.; Nakano, K. Enhanced photocatalytic activity of TiO_2/SiO_2 by the influence of Cu-doping under reducing calcination atmosphere. *Catal. Commun.* **2011**, *13*, 49–53. [CrossRef]
46. Nolan, M.; Watson, G.W. Hole localization in Al doped silica: A DFT + *U* description. *J. Chem. Phys.* **2006**, *125*, 144701. [CrossRef] [PubMed]
47. Nolan, M.; Watson, G.W. The electronic structure of alkali doped alkaline earth metal oxides: Li doping of MgO studied with DFT-GGA and GGA + *U*. *Surf. Sci.* **2005**, *586*, 25–37. [CrossRef]
48. Carey, J.J.; Nolan, M. Dissociative adsorption of methane on the Cu and Zn doped surface of CeO_2. *Appl. Catal. B* **2016**, *197*, 324–336. [CrossRef]
49. Nolan, M.; Elliott, S.D. The *p*-type conduction mechanism in Cu_2O: A first principles study. *Phys. Chem. Chem. Phys.* **2006**, *8*, 5350–5358. [CrossRef] [PubMed]
50. Morgan, B.J.; Watson, G.W. A DFT + *U* description of oxygen vacancies at the TiO_2 rutile (1 1 0) surface. *Surf. Sci.* **2007**, *601*, 5034–5041. [CrossRef]
51. Nolan, M.; Elliott, S.D.; Mulley, J.S.; Bennett, R.A.; Basham, M.; Mulheran, P. Electronic structure of point defects in controlled self-doping of the TiO_2 surface: Combined photoemission spectroscopy and density functional theory study. *Phys. Rev. B* **2008**, *77*, 235424. [CrossRef]
52. Kowalski, P.M.; Camellone, M.F.; Nair, N.N.; Meyer, B.; Marx, D. Charge localization dynamics induced by oxygen vacancies on the TiO_2 surface. *Phys. Rev. Lett.* **2010**, *105*, 146405. [CrossRef] [PubMed]
53. Morgan, B.J.; Watson, G.W. Polaronic trapping of electrons and holes by native defects in anatase TiO_2. *Phys. Rev. B* **2009**, *80*, 233102. [CrossRef]
54. Henkelman, G.; Arnaldsson, A.; Jónsson, H. A fast and robust algorithm for Bader decomposition of charge density. *Comput. Mater. Sci.* **2006**, *36*, 354–360. [CrossRef]
55. Scherrer, P. Estimation of the size and internal structure of colloidal particles by means of röntgen. *Nachr. Ges. Wiss. Göttingen* **1918**, *2*, 96–100.
56. Panneri, S.; Ganguly, P.; Mohan, M.; Nair, B.N.; Mohamed, A.A.P.; Warrier, K.G.; Hareesh, U.S. Photoregenerable, Bifunctional Granules of Carbon-Doped g-C_3N_4 as Adsorptive Photocatalyst for the Efficient Removal of Tetracycline Antibiotic. *ACS Sustain. Chem. Eng.* **2017**, *5*, 1610–1618. [CrossRef]
57. Wang, Y.; Zhang, R.; Li, J.; Li, L.; Lin, S. First-principles study on transition metal-doped anatase TiO_2. *Nanoscale Res. Lett.* **2014**, *9*, 46. [CrossRef] [PubMed]
58. Navas, J.; Sánchez-Coronilla, A.; Aguilar, T.; Hernández, N.C.; Desireé, M.; Sánchez-Márquez, J.; Zorrilla, D.; Fernández-Lorenzo, C.; Alcántara, R.; Martín-Calleja, J. Experimental and theoretical study of the electronic properties of Cu-doped anatase TiO_2. *Phys. Chem. Chem. Phys.* **2014**, *16*, 3835–3845. [CrossRef] [PubMed]
59. Zhang, H.; Yu, X.; McLeod, J.A.; Sun, X. First-principles study of Cu-doping and oxygen vacancy effects on TiO_2 for water splitting. *Chem. Phys. Lett.* **2014**, *612*, 106–110. [CrossRef]
60. Guo, M.; Du, J. First-principles study of electronic structures and optical properties of Cu, Ag, and Au-doped anatase TiO_2. *Physica B* **2012**, *407*, 1003–1007. [CrossRef]
61. Maimaiti, Y.; Nolan, M.; Elliott, S.D. Reduction mechanisms of the CuO (111) surface through surface oxygen vacancy formation and hydrogen adsorption. *Phys. Chem. Chem. Phys.* **2014**, *16*, 3036–3046. [CrossRef] [PubMed]
62. Assadi, M.H.N.; Hanaor, D.A. The effects of copper doping on photocatalytic activity at planes of anatase TiO_2: A theoretical study. *Appl. Surf. Sci.* **2016**, *387*, 682–689. [CrossRef]

63. Zhang, W.; Yin, J.-R.; Tang, X.-Q.; Zhang, P.; Ding, Y.-H. Density functional theory studies on the structural and physical properties of Cu-doped anatase TiO_2 surface. *Physica E* **2017**, *85*, 259–263. [CrossRef]
64. Duhalde, S.; Vignolo, M.F.; Golmar, F.; Chiliotte, C.; Torres, C.E.R.; Errico, L.A.; Cabrera, A.F.; Rentería, M.; Sánchez, F.H.; Weissmann, M. Appearance of room-temperature ferromagnetism in Cu-doped $TiO_{2-\delta}$ films. *Phys. Rev. B* **2005**, *72*, 161313. [CrossRef]
65. Iwaszuk, A.; Nolan, M. Charge compensation in trivalent cation doped bulk rutile TiO_2. *J. Phys.* **2011**, *23*, 334207. [CrossRef] [PubMed]
66. Du, M.-H.; Zhang, S.B. Impurity-bound small polarons in ZnO: Hybrid density functional calculations. *Phys. Rev. B* **2009**, *80*, 115217. [CrossRef]
67. Scanlon, D.O.; Walsh, A.; Morgan, B.J.; Nolan, M.; Fearon, J.; Watson, G.W. Surface sensitivity in lithium-doping of MgO: A density functional theory study with correction for on-site Coulomb interactions. *J. Phys. Chem. C* **2007**, *111*, 7971–7979. [CrossRef]
68. Schirmer, O.F. O–bound small polarons in oxide materials. *J. Phys.* **2006**, *18*, R667. [CrossRef]
69. Stoneham, A.M.; Gavartin, J.; Shluger, A.L.; Kimmel, A.V.; Ramo, D.M.; Rønnow, H.M.; Aeppli, G.; Renner, C. Trapping, self-trapping and the polaron family. *J. Phys.* **2007**, *19*, 255208. [CrossRef]
70. Chen, Y.-F.; Lee, C.-Y.; Yeng, M.-Y.; Chiu, H.-T. The effect of calcination temperature on the crystallinity of TiO_2 nanopowders. *J. Cryst. Growth* **2003**, *247*, 363–370. [CrossRef]
71. Ako, R.T.; Ekanayake, P.; Young, D.J.; Hobley, J.; Chellappan, V.; Tan, A.L.; Gorelik, S.; Subramanian, G.S.; Lim, C.M. Evaluation of surface energy state distribution and bulk defect concentration in DSSC photoanodes based on Sn, Fe, and Cu doped TiO_2. *Appl. Surf. Sci.* **2015**, *351*, 950–961. [CrossRef]
72. Jaiswal, R.; Bharambe, J.; Patel, N.; Dashora, A.; Kothari, D.; Miotello, A. Copper and Nitrogen co-doped TiO_2 photocatalyst with enhanced optical absorption and catalytic activity. *Appl. Catal. B* **2015**, *168*, 333–341. [CrossRef]
73. Sinatra, L.; LaGrow, A.P.; Peng, W.; Kirmani, A.R.; Amassian, A.; Idriss, H.; Bakr, O.M. A Au/Cu_2O–TiO_2 system for photo-catalytic hydrogen production. A pn-junction effect or a simple case of in situ reduction? *J. Catal.* **2015**, *322*, 109–117. [CrossRef]
74. Ganesh, I.; Kumar, P.P.; Annapoorna, I.; Sumliner, J.M.; Ramakrishna, M.; Hebalkar, N.Y.; Padmanabham, G.; Sundararajan, G. Preparation and characterization of Cu-doped TiO_2 materials for electrochemical, photoelectrochemical, and photocatalytic applications. *Appl. Surf. Sci.* **2014**, *293*, 229–247. [CrossRef]
75. Dashora, A.; Patel, N.; Kothari, D.; Ahuja, B.; Miotello, A. Formation of an intermediate band in the energy gap of TiO_2 by Cu–N-codoping: First principles study and experimental evidence. *Sol. Energy Mater. Sol. Cells* **2014**, *125*, 120–126. [CrossRef]
76. Jung, M.; Hart, J.N.; Scott, J.; Ng, Y.H.; Jiang, Y.; Amal, R. Exploring Cu oxidation state on TiO_2 and its transformation during photocatalytic hydrogen evolution. *Appl. Catal. A* **2016**, *521*, 190–201. [CrossRef]
77. Hu, Q.; Huang, J.; Li, G.; Jiang, Y.; Lan, H.; Guo, W.; Cao, Y. Origin of the improved photocatalytic activity of Cu incorporated TiO_2 for hydrogen generation from water. *Appl. Surf. Sci.* **2016**, *382*, 170–177. [CrossRef]
78. Parmigiani, F.; Pacchioni, G.; Illas, F.; Bagus, P. Studies of the CuO bond in cupric oxide by X-ray photoelectron spectroscopy and ab initio electronic structure models. *J. Electron Spectrosc. Relat. Phenom.* **1992**, *59*, 255–269. [CrossRef]
79. Hu, Q.; Huang, J.; Li, G.; Chen, J.; Zhang, Z.; Deng, Z.; Jiang, Y.; Guo, W.; Cao, Y. Effective water splitting using $CuOx/TiO_2$ composite films: Role of Cu species and content in hydrogen generation. *Appl. Surf. Sci.* **2016**, *369*, 201–206. [CrossRef]
80. Shannon, R.D. Revised effective ionic radii and systematic studies of interatomic distances in halides and chalcogenides. *Acta Crystallogr. Sect. A* **1976**, *32*, 751–767. [CrossRef]
81. Kubacka, A.; Munoz-Batista, M.; Fernández-García, M.; Obregón, S.; Colón, G. Evolution of H_2 photoproduction with Cu content on $CuOx$-TiO_2 composite catalysts prepared by a microemulsion method. *Appl. Catal. B* **2015**, *163*, 214–222. [CrossRef]
82. Aguilera-Ruiz, E.; García-Pérez, U.M.; de la Garza-Galván, M.; Zambrano-Robledo, P.; Bermúdez-Reyes, B.; Peral, J. Efficiency of $Cu_2O/BiVO_4$ particles prepared with a new soft procedure on the degradation of dyes under visible-light irradiation. *Appl. Surf. Sci.* **2015**, *328*, 361–367. [CrossRef]
83. Siripala, W.; Ivanovskaya, A.; Jaramillo, T.F.; Baeck, S.-H.; McFarland, E.W. A Cu_2O/TiO_2 heterojunction thin film cathode for photoelectrocatalysis. *Sol. Energy Mater. Sol. Cells* **2003**, *77*, 229–237. [CrossRef]

84. Scanlon, D.O.; Dunnill, C.W.; Buckeridge, J.; Shevlin, S.A.; Logsdail, A.J.; Woodley, S.M.; Catlow, C.R.A.; Powell, M.J.; Palgrave, R.G.; Parkin, I.P.; et al. Band alignment of rutile and anatase TiO_2. *Nat. Mater.* **2013**, *12*, 798. [CrossRef] [PubMed]
85. Chen, L.; Tang, M.; Chen, C.; Chen, M.; Luo, K.; Xu, J.; Zhou, D.; Wu, F.J.E.S. Technology, Efficient bacterial inactivation by transition metal catalyzed auto-oxidation of sulfite. *Environ. Sci. Technol.* **2017**, *51*, 12663–12671. [CrossRef] [PubMed]
86. Ganguly, P.; Byrne, C.; Breen, A.; Pillai, S.C. Antimicrobial activity of photocatalysts: Fundamentals, mechanisms, kinetics and recent advances. *Appl. Catal. B* **2018**, *225*, 51–75. [CrossRef]



© 2018 by the authors. Licensee MDPI, Basel, Switzerland. This article is an open access article distributed under the terms and conditions of the Creative Commons Attribution (CC BY) license (http://creativecommons.org/licenses/by/4.0/).